



## OPEN Mechanism and CO<sub>2</sub> emissions analysis of multi-solid-waste synergistic red mud-based composite cementitious materials under orthogonal tests

Lili Cheng<sup>1✉</sup>, Daiyu Zhou<sup>2</sup>, Qiwan Zhang<sup>1</sup>, Lingling Wang<sup>2</sup>, Ninggui Hu<sup>2</sup> & Zeyuan Wang<sup>2</sup>

The large stockpile and low utilization rate of red mud (RM) have caused an urgent need for large quantities of RM to be eliminated. In this study, multi-solid-waste synergistic RM-based composite cementitious materials (MS-RMCM) were prepared using RM as the primary material, combined with fly ash, silica fume, and quicklime. Orthogonal tests were conducted to investigate the effects of cementitious components on the mechanical properties. The effect mechanisms were discussed by SEM–EDS results. The results revealed that: (1) Range analysis indicated that the factors influencing the 28 d compressive strength ranked as follows: quicklime (C) > silica fume (B) > fly ash (A). The optimal combination was determined to be A<sub>2</sub>B<sub>3</sub>C<sub>4</sub>, achieving a maximum compressive strength of 25.13 MPa with 53% RM. (2) Variance analysis revealed that  $F(\text{fly ash}) = 3.961 < F_{0.01}$ ,  $F(\text{silica fume}) = 17.778 > F_{0.01}$ , and  $F(\text{quicklime}) = 61.921 > F_{0.01}$ , indicating that fly ash had no significant effect on the 28 d compressive strength, while silica fume had a significant effect, and quicklime had a highly significant effect. (3) Microscopic analysis showed that the strength improvement contributed by fly ash and silica fume was mainly attributed to their good potential pozzolanic activity and microaggregate filling effect. Quicklime enhanced the compactness by generating more hydration products after activating fly ash, silica fume and RM. (4) Life cycle assessment calculations indicated that the carbon emissions of MS-RMCM were 273.01 kg/t, with a unit compressive strength carbon emission coefficient of 10.86 kg/MPa, indicating the significant advantages of MS-RMCM in reducing CO<sub>2</sub> emissions in the construction industry.

**Keywords** Red mud, Multi-solid-waste, Mechanical strength, Carbon emissions, synergistic mechanism

### List of symbols

RM	Red mud
C–A–H	Calcium aluminate hydrate
RMCM	Red mud-based composite materials
SEM	Scanning electron microscopy
EDS	Energy dispersive spectroscopy
C–S–H	Calcium silicate hydrate
C–A–F–H	Calcium aluminates ferrite hydrate
MS-RMCM	Multi-solid-waste synergistic RM-based composite cementitious materials
SCO <sub>2</sub>	Total carbon emissions
ACO <sub>2</sub>	Emissions during acquisition
TCO <sub>2</sub>	Emissions during transportation
PCO <sub>2</sub>	Emissions during preparation
RM-WGS	RM and waste glass sludge
RM-GGBS	RM and ground granulated blast-furnace slag

<sup>1</sup>Department of Civil Engineering, Guiyang Institute of Information Science and Technology, Guiyang 550025, Guizhou, China. <sup>2</sup>College of Civil Engineering, Guizhou University, Guiyang 550025, Guizhou, China. ✉email: Lilycheng1231@163.com

RS RM-based sulphoaluminate cementitious materials  
 RM-SAC RM based sulphoaluminate cement

Red mud (RM), an industrial solid waste and byproduct of alumina production from bauxite, was generated at an average rate of 1.25 tons per ton of alumina<sup>1</sup>. At present, the global storage capacity of RM has been nearly 4 billion tons<sup>2</sup>. However, the strong alkalinity, high impurity content, and complex mineral composition of RM made large-scale comprehensive utilization challenging<sup>3,4</sup>. Stockpiling RM not only occupied a large amount of land, but also caused different degrees of harm to the soil, water, atmosphere and human beings<sup>5,6</sup>. Meanwhile, RM was rich in calcium, silicon, aluminum and other silica-aluminate minerals<sup>7</sup>. The effective utilization of RM resource attributes will meet the requirements of circular economy development. In recent years, researchers have done a lot of research around the utilization of RM, and found that RM had a better application prospect in extraction of valuable metals<sup>8</sup>, construction materials<sup>9</sup>, chemical production<sup>10</sup> and environment and agriculture<sup>11</sup>. The resources utilization status of RM in China is shown in Fig. 1. It can be observed that the resources utilization rate of RM in the aforementioned sectors was 18%, 33%, 25%, and 20% respectively. Although RM showed potential application prospects in metallurgy, chemical production and environmental protection, the utilization ratio of RM is less than 5%<sup>6</sup> and it is far from being able to achieve large-scale resources utilization. Therefore, using RM to produce construction materials was widely regarded as the optimal approach.

Red mud-based composite materials (RMCM) are not only consumed a large amount of RM, but also reduced the consumption of cement, construction costs and carbon emissions. Experts and scholars have done a lot of researches on the basic properties, activation and practical application of RM. Relevant researches<sup>1,2,6,12</sup> results showed that RM was rich in Si and Al elements, and contained CaO and Na<sub>2</sub>O. RM could undergo a slow hydration reaction, but the cementitious properties were not significant, because of its low content of active silica-alumina. In order to improve the activity of RM, Wei<sup>13</sup> and Jiang<sup>14</sup> used mechanical ball milling to activate RM physically, and the 3 days (d) and 7 d compressive strength increased by 0.21 MPa and 0.49 MPa, respectively. Although the strength of RM specimens had some improvement, it was far from meeting the demand of engineering application, and the water consumption increased significantly. Thermal activation was a method to remove free and bound water from RM by high temperature calcination. Then, bond breaking and activation points appeared in the structure, prompting the rearrangement of silica-aluminate minerals. RM was transformed from metastable structure to amorphous form. Thermal activation could improve the reactivity of RM, but it faced issues of high energy consumption, high cost, and complex process<sup>15–17</sup>. Chemical activation mostly used activators, such as water glass, gypsum and sodium hydroxide, to enhance the activity of SiO<sub>2</sub> and Al<sub>2</sub>O<sub>3</sub> in RM<sup>18,19</sup>, which was both environmentally friendly and economical. Moreover, chemical activation could simultaneously process multiple solid wastes and the most advantageous method on preparation of RMCM.

At present, the researches on multi-solid-waste synergistic red mud-based composite cementitious materials (MS-RMCM) focused on binary and multi-component systems. Liu et al.<sup>20</sup> activated RM through calcination and ball milling, then mixed with S95 slag powders to prepare cementitious material. The 28 d compressive and flexural strengths reached up to 40 MPa and 8 MPa after strengthened the activity of silica-alumina with water glass. Geng et al.<sup>21</sup> prepared cementitious materials by calcination at 800 °C containing RM and coal gangue, and the 7 d compressive strength was up to 14 MPa. Bao et al.<sup>22</sup> reported that the oil shale slag and RM after 700 °C calcination could prepare cementitious materials with 28 d compressive strength as high as 17.31 MPa. Previous studies have found that the binary RMCM can give full play to the advantages of SiO<sub>2</sub> and Al<sub>2</sub>O<sub>3</sub>, and obtain high compressive strength. However, the RM needed to be calcined at high temperature, which would cause the problem of high energy consumption and high cost.

MS-RMCM generally included alkaline solid waste (red mud, carbide slag), siliceous solid waste (silica fume, glass powder), silica-alumina solid waste (fly ash, slag), gypsum solid waste (phosphogypsum, desulfurization gypsum) and quicklime. Among them, alkaline solid waste provided the alkaline environment to promote the hydrolysis, and gypsum solid waste mainly facilitated the formation of hydration products<sup>23</sup>. Li et al.<sup>24</sup> prepared ternary cementitious materials of RM-fly ash-desulfurization gypsum, and found that the 7 d compressive strength (5.49 MPa) was higher than that of RM-fly ash (4.25 MPa) and RM-desulfurization gypsum (3.73 MPa). Luo et al.<sup>25</sup> analyzed the effect of blast furnace slag, chromium slag, RM on the early compressive strength, and

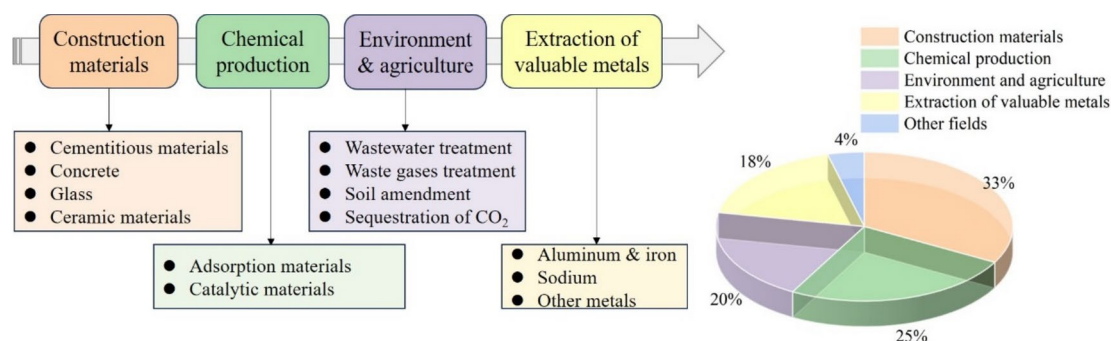


**Fig. 1.** Resources utilization status of red mud in China.

Constituent materials	CaO	SiO <sub>2</sub>	Fe <sub>2</sub> O <sub>3</sub>	Al <sub>2</sub> O <sub>3</sub>	SO <sub>3</sub>	Na <sub>2</sub> O	MgO	K <sub>2</sub> O	TiO <sub>2</sub>	Others
RM	31.12	18.63	14.42	13.72	–	13.35	2.8	0.22	4.83	0.91
Cement	61.71	19.90	4.46	5.16	3.96	–	1.73	1.20	–	1.88
Quicklime	98.29	0.60	0.11	0.14	0.24	–	–	0.58	–	0.04
Silica fume	0.48	97.60	0.07	0.81	0.46	–	0.21	–	–	0.37
Fly ash	7.58	52.65	9.22	18.89	1.89	–	5.11	–	–	4.66

**Table 1.** Chemical compositions of RM and admixtures (%).

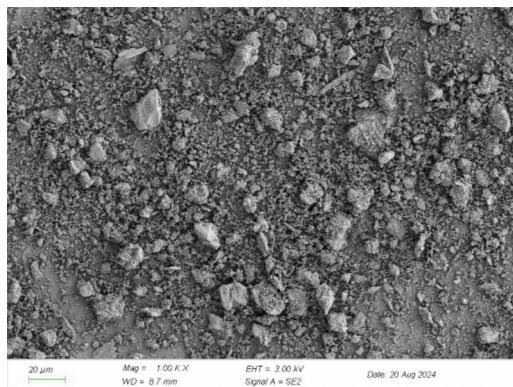


**Fig. 2.** Micro-morphology of RM.

prepared ternary cementitious materials, which 7 d compressive strength was 15.73 MPa. In the study of Wang et al.<sup>26</sup>, the compressive strength of multi-component solid waste low-carbon cementitious materials reached 35 MPa, which was superior to the mechanical properties of P.O.32.5 cement. R. Kirthiga et al.<sup>27</sup> focused on potential utilization of sugarcane bagasse ash as agricultural waste and silica fume as industrial waste to develop cement-based mortar. Ding et al.<sup>28</sup> conducted a solidification experiment of RM with fly ash, lime, and clay. The results showed that with the increase of lime proportion in the two-ash ratio, the strength of all ages increased, of which the 28 d strength was the most significantly affected by the two-ash ratio. He et al.<sup>29</sup> added slag and silica fume into RM activated by NaOH. They found that both single and combined addition of slag and silica fume could improve the strength of solidified RM. The effect of combined addition was more significant, and the compressive strength of 28 d reached 13.12 MPa. In conclusion, MS-RMCM effectively utilized the active chemical components of various solid wastes to enhance the mechanical properties of the materials. Additionally, the higher incorporation of industrial solid wastes helped to reduce preparation costs. However, although the above studies achieved synergistic benefits, the overall RM dosage was not significant, and the mechanical properties were poor at higher dosage of RM. Moreover, studies on the systematic mechanism were relatively limited.

This study used RM after low-temperature roasting as the main raw material to prepare MS-RMCM. Fly ash and silica fume were added, and quicklime was incorporated for chemical activation. The effects and significance of each cementitious component on flexural and compressive strengths were investigated through orthogonal tests. The optimal level of each cementitious component and the optimal ratio were obtained. In addition, the synergistic mechanisms were revealed by scanning electron microscopy (SEM) and energy dispersive spectroscopy (EDS) results. The results of this study provided a basis for the selection of mineral admixtures in MS-RMCM and laid a foundation for the resources utilization and large-scale disposal of RM.

## Experiment

### Experimental materials

RM was obtained from an alumina factory in Guizhou, China. After natural air drying and crushing, the RM powders were obtained through 0.6 mm hole sieving, and baked in the oven at 105 °C for 5 h to obtain the raw RM powders. The cement P.O.42.5 produced in the Guiyang Conch Panjiang Cement Plant, and quicklime was selected with 98.3% CaO. Silica fume was used with SiO<sub>2</sub> content greater than 97% and a specific surface area of 20–28 m<sup>2</sup>/g. Additionally, F10 melamine water reducer was used in this study and the water-reducing rate is 16%–22%. The chemical compositions of RM and the other admixtures are provided in Table 1.

The microscopic morphology of the raw RM powders is shown in Fig. 2. It can be seen from the SEM image that RM is scattered and the particle size is various. The shape of RM is diversified and not fixed. The particle size distribution of RM is shown in Fig. 3. In the cumulative curve, the particle size of 80% RM is less than 300 μm.

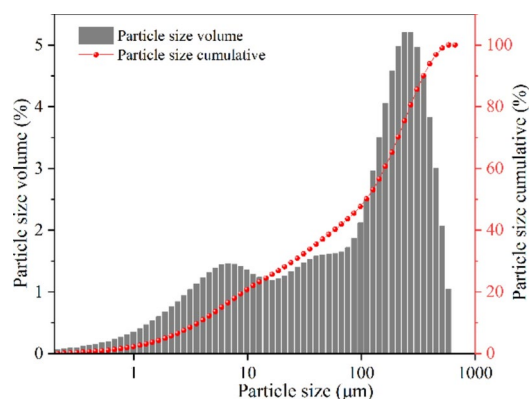


**Fig. 3.** Particle size distribution of RM.

Sample number	Factors (%)		
	Fly ash (A)	Silica fume (B)	Quicklime (C)
1	10	2	4
2	10	4	8
3	10	6	12
4	10	8	16
5	15	2	8
6	15	4	4
7	15	6	16
8	15	8	12
9	20	2	12
10	20	4	16
11	20	6	4
12	20	8	8
13	25	2	16
14	25	4	12
15	25	6	8
16	25	8	4

**Table 2.** Level of factors in orthogonal tests.

### Test design

In this study, RM was used as the main material. MS-RMCM was prepared by adding a certain proportion of mineral admixtures such as fly ash, silica fume and quicklime, as well as water reducer into RM. In order to ensure the early strength, the cement dosage was fixed at 10%, and the sum of the remaining powder was 90%. By changing the blending ratio of fly ash, silica fume and quicklime, the orthogonal tests were designed to explore the effect of mineral admixtures on the flexural and compressive strengths. Based on the study by Liu et al.<sup>14,30,31</sup>, the dosage of fly ash, silica fume and quicklime were determined to be 10–25%, 2–8% and 4–16%, respectively. The dosage of water reducer was established as 1% of the total mass of dry powders, and the water-to-binder ratio was taken as 0.4.

Orthogonal test is a scientific method for studying multi-factor and multi-level optimization. By applying the orthogonal principle of orthogonal tables and mathematical statistical analysis, it scientifically selects representative combinations from numerous experimental possibilities for testing, thereby optimizing the relevant performance indicators<sup>32</sup>. Considering the complexity of the experimental factors and the mixed levels in this study, it was difficult to maintain experiment quality. Orthogonal tests were utilized to minimize the number of tests to evaluate the effects of various factors on the mechanical properties of MS-RMCM at different curing ages, facilitating the selection of parameter combinations with optimal mechanical performance<sup>33</sup>. Minitab and SPSS software were employed to design a three-factor (A, B, C), four-level (1, 2, 3, 4) orthogonal test, with data analyzed through methods such as intuitive analysis, range analysis, and variance analysis. The mix ratio design of the orthogonal tests is shown in Table 2.

The preparation and test procedure of specimens are shown in Fig. 4. The RM, cement, fly ash, silica fume, quicklime and water reducer were mixed and stirred at 100 r/min for 30 s until the dry powders were uniformly blended. Water was slowly added, and mixing was continued at 100 r/min for 60 s, followed by 30 s of mixing at 600 r/min, to ensure complete integration of water and dry powders. The mixed slurry was poured into

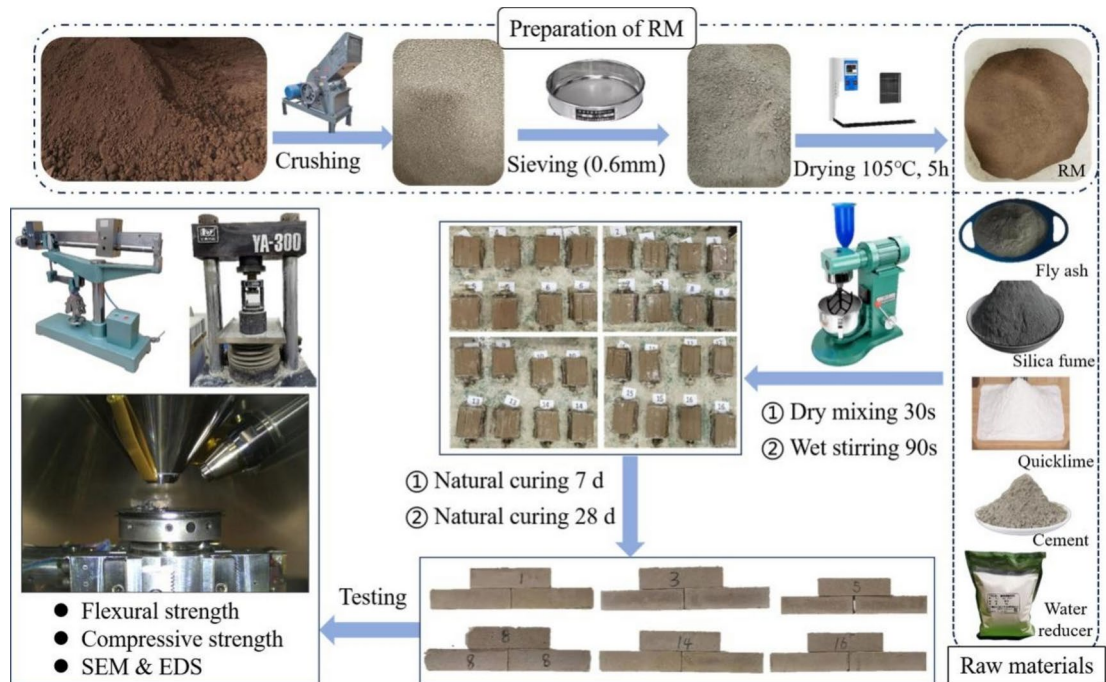


**Fig. 4.** Preparation and test process.

the 40 mm × 40 mm × 160 mm triple molds pre-impregnated release agent, vibrated to eliminate air bubbles, smoothed with the steel rule, and covered with plastic film to avoid the loss of water. The samples were demolded after 24 h of curing in natural environment. The tests were carried out after the natural curing to the age of 7 d and 28 d.

### Test methods

The mechanical properties were characterized by flexural strength and compressive strength, which were determined according to Chinese standard GB/T17671-2021 "Cement Mortar Strength Inspection Method". Three specimens were selected for strength testing in each experimental mix proportion. The flexural strength test was determined using the three-point bending method and carried out by an electric flexural testing machine. The specimens were placed in the flexural fixture, and after adjusting and calibrating the relevant parameters, they were loaded at a rate of 50 N/s. The specimens tested for flexural strength were then used for compressive strength testing. They were positioned in the compressive strength fixture of a digitally electro-hydraulic servo pressure testing machine, and after parameter adjustment and calibration, the specimens were loaded at a rate of 2400 N/s. The microstructures of samples were characterized by SEM–EDS. After the compressive strength tests, a sample not exceeding 1 cm<sup>3</sup> was taken from the middle part of the specimen. After drying and spraying gold treatment on the surface, the sample was subjected to SEM testing.

## Results and discussion

### Intuitive analysis

Figure 5 presents the visual results of compressive and flexural strengths at 7 d and 28 d for the specimens under 16 mix ratios. It can be seen that, with the increase of curing age, both the flexural and compressive strengths of specimens show an increasing trend.

As shown in Fig. 5a, the 28 d compressive strength of group 7 reached the maximum 25.13 MPa. Group 1 showed the lowest compressive strength, which was 10.10 MPa. This was attributed to the low activity and high dosage of RM in group 1 (up to 74%), which was unfavorable for the development of cementitious material strength. The increase of RM dosage led to a reduction in the Ca element content within the cementitious material, thereby decreasing the formation of hydration products<sup>34</sup>. In particular, group 16 showed a decline in 28 d compressive strength, which was ascribed to the low dosage of quicklime (minimum 4%), resulting in limited cementitious ability of the cementitious material. With the increase in curing age, the limited amount of quicklime restrained the alkali activation effect and confined the hydration reaction, resulting in a large amount of RM powders failing to fully release the cementitious activity. Simultaneously, the drying process during the curing period caused the RM slurry to lose the surface tension provided by water, which in turn intensified the dispersion between the particles and reduced the compactness of cementitious material. In terms of the average strength of the samples, the 7 d compressive strength reached 79.18% of the 28 d compressive strength, whereas the 7 d flexural strength only accounted for 44.30% of the 28 d flexural strength. This suggested that the compressive strength had essentially developed by 7 d, but the development of flexural strength was relatively slow. From the strength ratio of 7 d and 28 d (7d/28d), the fluctuation range of the compressive strength ratios

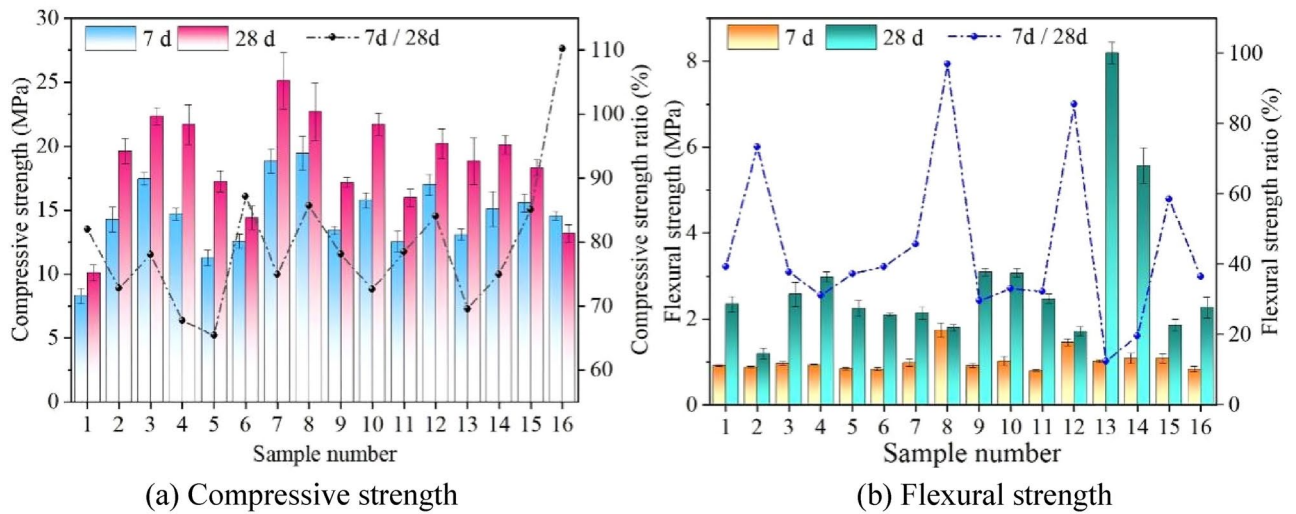


Fig. 5. Results of orthogonal tests.

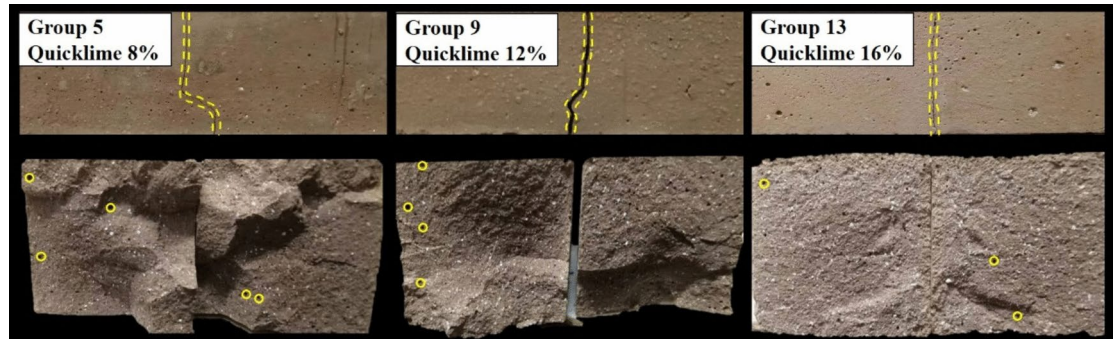


Fig. 6. Flexural failure modes of MS-RMCM.

was primarily concentrated between 65 and 90%, while the fluctuation range of the flexural strength ratios was distributed between 25 and 60%. Thus, it was observed that the stability of compressive strength exceeded that of flexural strength. Notably, the 7 d flexural strength of group 13 was only 12.39% of the 28d strength, while the 28 d flexural strength reached the maximum value of 8.19 MPa in this test. This could be explained by the higher sensitivity of flexural strength to fluctuations compared with compressive strength. Additionally, this group had the highest proportion of silica fume, fly ash, and quicklime, with a larger amount of supplementary cementitious materials effectively promoting the hydration reaction. In this case, the relatively low dosage of RM (minimum 47%) indicated that excessive RM was detrimental to the mechanical strength, which was consistent with Liu's conclusion<sup>35</sup>. Furthermore, the higher dosage of quicklime (maximum 16%) enhanced the alkali activation effect of RM, resulting in more complete hydration reactions within the cementitious material. The above analysis was also verified in the 28 d flexural failure modes of the MS-RMCM samples, as shown in Fig. 6.

It can be seen from the Fig. 6 that longitudinal cracks developed after the samples failed, exhibiting typical brittle failure. As the dosage of quicklime increased, the deflection of crack gradually disappeared, the fracture surface became flat, and the local fracture features transitioned from irregular to smooth. Specifically, when the quicklime dosage reached 16%, the vertical surface cracks appeared, and the fractural cross-section was smooth and regular.

This was because the lower dosage of quicklime resulted in the low concentration of  $\text{OH}^-$ , reducing the alkaline activation effect. Thus, the activation effect of RM was limited under the lower dosage of quicklime and higher dosage of RM, which led to uneven hydration reaction, decreasing the local bond strength. Therefore, cracks would appear the deflection near the concentrated hydration crystals. The lower bond strength between the concentrated hydration crystals and matrix caused the relatively lower flexural and compressive strengths. The more significant concentration of hydration crystals in Group 5 caused more significant cracks deflection and poorer surface smoothness. With the increase of quicklime, the activation effect of RM enhanced, reducing the concentration of hydration crystals in the local regions. Moreover, the increase of silica fume and fly ash further enhanced active effect of cementitious components, causing the relatively uniform distribution of hydration products. Consequently, the specimen of group 13 with 16% quicklime exhibited the higher compactness and relatively smoother fracture surface. As a result, the flexural strength increased from 2.25 MPa to 8.19 MPa, as the

Sample number	Fly ash (A)	Silica fume (B)	Quicklime (C)
1	0.63	0.12	0.25
2	0.46	0.18	0.36
3	0.36	0.21	0.43
4	0.29	0.24	0.47
5	0.60	0.08	0.32
6	0.66	0.17	0.17
7	0.41	0.16	0.43
8	0.43	0.23	0.34
9	0.59	0.06	0.35
10	0.50	0.10	0.40
11	0.67	0.20	0.13
12	0.56	0.22	0.22
13	0.58	0.05	0.37
14	0.61	0.10	0.29
15	0.64	0.15	0.21
16	0.68	0.22	0.10

**Table 3.** Normalization of mix proportion for the orthogonal tests.

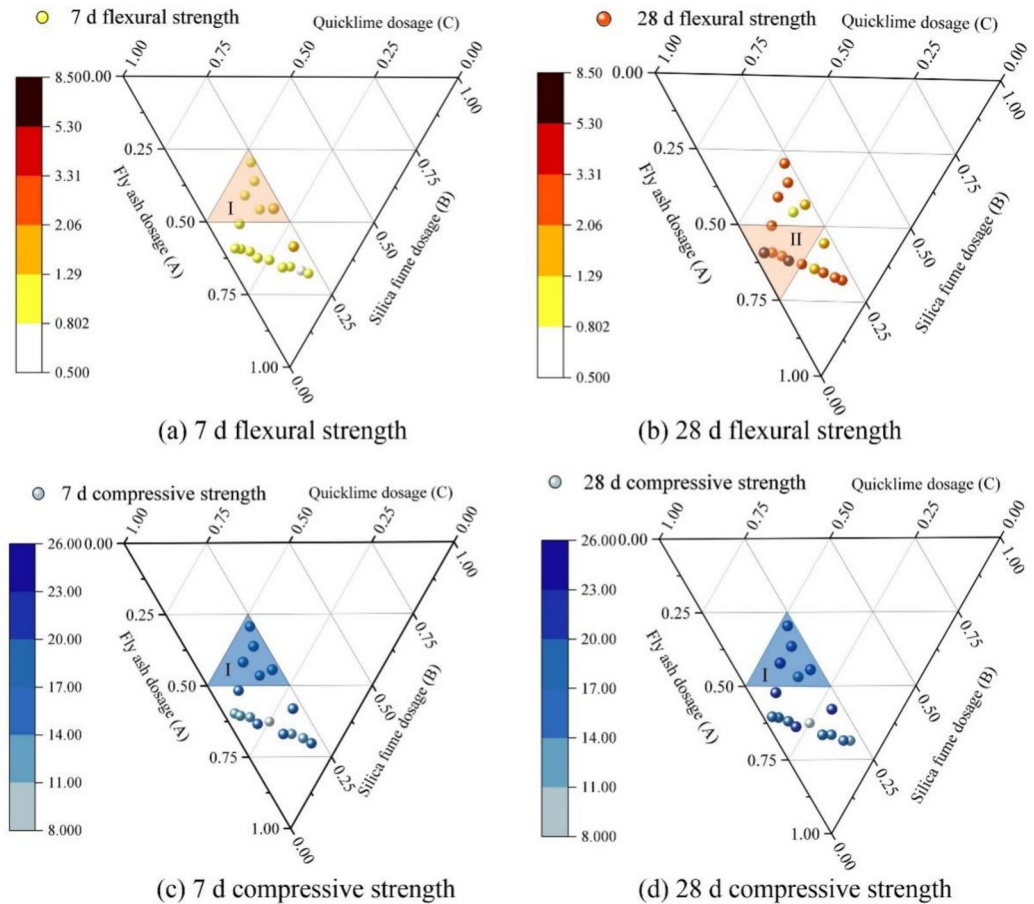


**Fig. 7.** Three-phase impact diagram of the orthogonal tests.

dosage of quicklime increased from 8 to 16%. In addition, as shown in the Fig. 6, increasing the quicklime dosage contributed to a reduction in the number of pores, which confirmed that the improvement in the compactness of cementitious material.

The results of further normalization of orthogonal tests are shown in Table 3. Three-phase impacts of the orthogonal test factors (A, B, C) on flexural and compressive strengths were established, as shown in Fig. 7.

Level	A	B	C	A	B	C	A	B	C	A	B	C
	7 d flexural strength			28 d flexural strength			7 d compressive strength			28 d compressive strength		
K1	0.93	0.92	0.84	2.27	3.97	2.30	13.67	11.51	11.98	18.44	15.83	13.42
K2	1.10	0.95	1.07	2.07	2.98	1.75	15.53	14.42	14.52	19.87	18.96	18.83
K3	1.05	0.96	1.18	2.58	2.26	3.26	14.67	16.09	16.34	18.76	20.44	20.58
K4	1.01	1.24	0.99	4.47	2.19	4.10	14.57	16.41	15.59	17.60	19.44	21.83
R	0.17	0.32	0.34	2.40	1.78	2.34	1.85	4.90	4.37	2.27	4.61	8.42

**Table 4.** Characteristic parameters for the range analysis.

Results	7 d flexural strength	28 d flexural strength	7 d compressive strength	28 d compressive strength
Significance	C > B > A	A > C > B	B > C > A	C > B > A
Optimum combination	A <sub>2</sub> B <sub>4</sub> C <sub>3</sub>	A <sub>4</sub> B <sub>1</sub> C <sub>4</sub>	A <sub>2</sub> B <sub>4</sub> C <sub>3</sub>	A <sub>2</sub> B <sub>3</sub> C <sub>4</sub>

**Table 5.** Results of the range analysis.

The optimal flexural strength at 7 d and 28 d appeared in zone I and zone II, respectively, while the optimal compressive strengths at both 7 d and 28 d were found in zone I. This confirmed that the fluctuation sensitivity of flexural strength was greater than that of compressive strength. Upon comparing the strength of 7 d and 28 d, it was found that as the curing age increased, the development of flexural strength was considerably superior to that of compressive strength.

### Range analysis

The range analysis method, abbreviated as the R method, is employed to evaluate the results of orthogonal tests. The flexural and compressive strengths were used as evaluation indices for range analysis.

Define  $X_{mn}$  as the  $m$ -th level value of the influencing factor  $n$  ( $m = 1, 2, 3, 4$ ;  $n = A, B, C$ ).  $Y_{mnk}$  represents the evaluation index value corresponding to the  $m$ -th level of  $n$  factor.  $N$  orthogonal tests are carried out under  $X_{mn}$ , resulting in  $N$  values, denoted as  $Y_{mnk}$  ( $k = 1, 2, \dots, N$ ). The values of  $K$  and  $R$  are calculated by the below Eqs.<sup>32,33</sup>

$$K_{mn} = \frac{1}{N} \sum_{k=1}^N Y_{mnk} \quad (1)$$

$$R_n = \max \{K_{1n}, K_{2n}, K_{3n}, K_{4n}\} - \min \{K_{1n}, K_{2n}, K_{3n}, K_{4n}\} \quad (2)$$

In the equations,  $K_{mn}$  represents the average value of influencing factor  $n$  at the  $m$ -th level;  $R_n$  denotes the range value of the factor  $n$ .

The results of flexural and compressive strengths shown in Fig. 5 were processed using SPSS software, and the results of characteristic parameters were presented in Table 4. Based on the results of Table 4, the influence of each factor on the index was determined according to the value of  $R$ , and the optimal levels and combinations of factors were identified based on the  $K$  values. The results are shown in Table 5. In the results of the orthogonal tests, the larger  $R$  value of a factor represents the greater influence on the evaluation indicators. A larger  $K$  value indicates that the factor exhibits optimal performance at that corresponding level. Based on the data results, it was observed that the effect of different cementitious components on the flexural and compressive strengths changed with the curing age. In particular, fly ash had an overall insignificant effect on the strength of MS-RMCM. The effect of each factor on the 28 d compressive strength was ranked as follows: quicklime (C) > silica fume (B) > fly ash (A). The optimal combination was determined to be A<sub>2</sub>B<sub>3</sub>C<sub>4</sub>. For the 28 d flexural strength, the effect was ranked as follows: fly ash (A) > quicklime (C) > silica fume (B), with the optimal combination identified as A<sub>4</sub>B<sub>1</sub>C<sub>4</sub>.

In order to visually illustrate the effect of different factors on the flexural and compressive strengths of MS-RMCM, the range values ( $R$ ) of each factor at different ages are shown in Fig. 8. The quicklime had a significant impact on both the 28 d flexural and compressive strengths. In particular, the  $R$  of 7 d flexural strength for silica fume (0.32) was very close to quicklime (0.34). Therefore, it is reasonable to say that silica fume and quicklime contributed nearly equally to the early flexural strength of MS-RMCM.

### Variance analysis

To further analyze the effects of fly ash, silica fume, and quicklime on the flexural and compressive strengths of MS-RMCM, variance analysis was conducted. The results were imported into SPSS software, where three-factor main effect variance analysis tables for each evaluation index were established. The results are shown in Table 6.

$F$  is used to evaluate the significance of one factor on the test results;  $F_{0.1}(3,6) = 3.29$ ;  $F_{0.05}(3,6) = 4.76$ ;  $F_{0.01}(3,6) = 9.78$ .  $F > F_{0.01}$  indicates that the factor is highly significant, marked as "\*\*\*";  $F_{0.01} > F > F_{0.05}$  indicates that the factor is significant, marked as "\*\*";  $F_{0.05} > F > F_{0.1}$  indicates that the factor has a certain level of effect; and factor with  $F < F_{0.1}$  has an insignificant effect.  $P$  is an indicator of reliability of the results. When  $P \leq 0.05$ ,

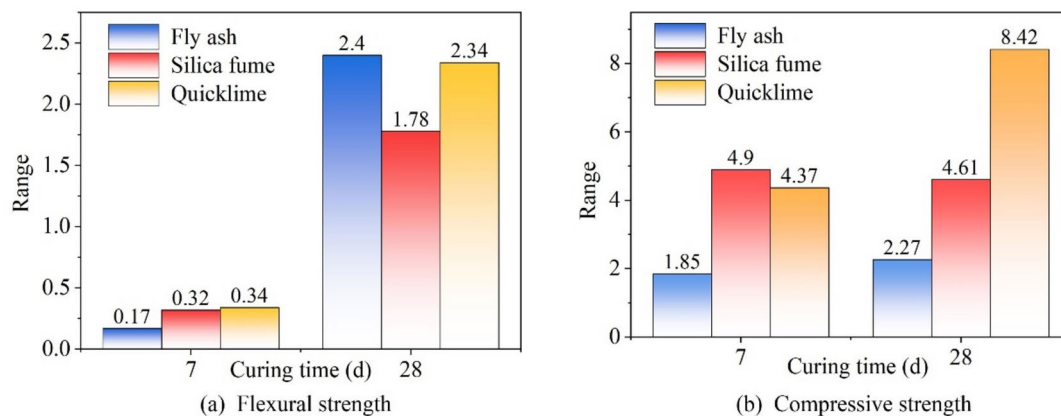


Fig. 8. Range of each factor.

Index	Factor	Sum of squares	Degree of freedom	Mean square	F	P	Significance
7 d flexural strength	A	0.063	3	0.021	0.348	0.793	B > C > A
	B	0.264	3	0.088	1.455	0.318	
	C	0.241	3	0.080	1.325	0.351	
28 d flexural strength	A	14.557	3	4.852	3.340	0.097	A > C > B
	B	8.217	3	2.739	1.885	0.233	
	C	12.907	3	4.302	2.961	0.120	
7 d compressive strength	A	6.900	3	2.300	1.372	0.338	B** > C* > A
	B	60.231	3	20.077	11.974	0.006	
	C	43.599	3	14.533	8.667	0.013	
28 d compressive strength	A	10.568	3	3.523	3.961	0.071	C** > B** > A
	B	47.428	3	15.809	17.778	0.002	
	C	165.194	3	55.065	61.921	<0.001	

Table 6. Variance analysis for orthogonal tests.

it indicates that the levels of this factor have significant difference; When  $P > 0.05$ , no significant difference is considered.

As shown in Table 6, the effects of all three factors on the flexural strength were not significant. Fly ash showed no significant effect on the 7 d compressive strength and only a moderate effect on the 28 d compressive strength, though the significance was not high. For silica fume,  $F > F_{0.01}$  and  $P < 0.01$ , indicating that the silica fume had a significant impact on compressive strength throughout the curing process. The F for quicklime at 7 d was between  $F_{0.05}$  and  $F_{0.01}$ , reflecting that quicklime had a certain effect on the 7 d compressive strength. At 28 d, the effect became highly significant, with  $F = 61.921 > F_{0.01}$  and  $P < 0.001$ . Overall, the conclusions from the variance analysis were almost consistent with those from the range analysis. Fly ash showed no significant effect on the compressive and flexural strengths of MS-RMCM. Silica fume had a highly significant effect on the compressive strength. Quicklime had a more noticeable significant effect on the 28 d compressive strength than on the 7 d compressive strength.

### Factors index analysis

#### Effect of cementitious components on the flexural strength

The effects of various cementitious components on the flexural strength of MS-RMCM are shown in Fig. 9. It can be observed that the effects of these components on the flexural strength at different curing ages vary significantly.

As shown in Fig. 9a, with the increase of fly ash, the 7 d flexural strength of the samples first increased and then decreased, while the 28 d flexural strength initially decreased and then increased. When the fly ash dosage reached 15%, the 7 d flexural strength reached its peak at 1.1 MPa. Increasing the fly ash dosage further resulted in a maximum fluctuation of only 0.09 MPa, indicating that the effect of fly ash on early flexural strength was relatively small. Figure 9b shows that as the silica fume dosage increased, the 7 d flexural strength increased gradually, while the 28 d flexural strength decreased progressively. The maximum fluctuation in the 7 d flexural strength at this point was 0.32 MPa, suggesting that although silica fume contributed to the improvement of early flexural strength, the extent of this improvement was small. When the silica fume dosage was 2%, the 28 d flexural strength was 3.97 MPa, and when the silica fume dosage increased to 8%, the flexural strength decreased by 44.88%. This indicated that silica fume was not conducive to the later flexural strength and its side effect was

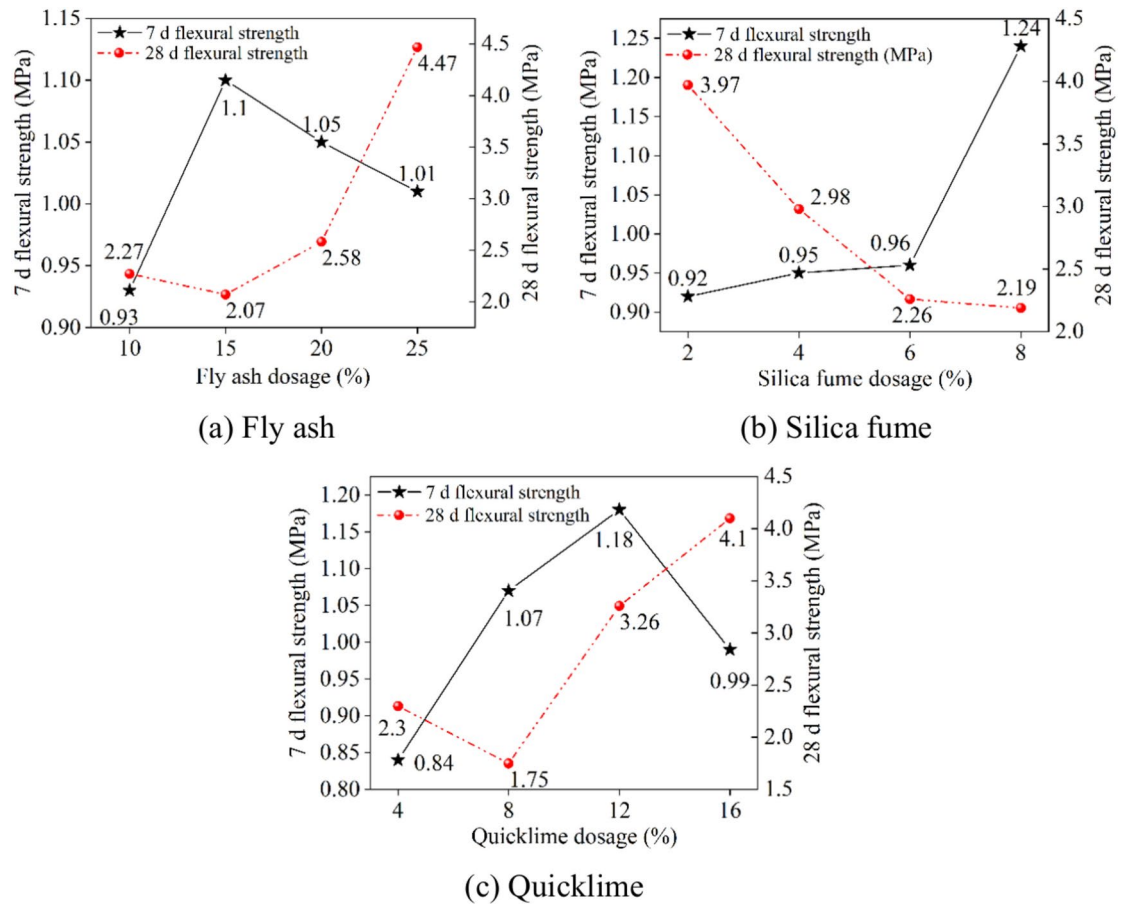


**Fig. 9.** Mean effect plots of 7 d and 28 d flexural strengths.

significant. The main reason was the larger specific surface area of the silica fume particles. During the early stages of hydration, sufficient  $\text{Ca}(\text{OH})_2$  facilitated the formation of C-S-H, improving the compactness of the cementitious material. However, as the hydration reaction proceeded, the  $\text{Ca}(\text{OH})_2$  was gradually consumed. With further increase in silica fume, the unreacted silica fume particles began to agglomerate, forming weakly hydrated zones and weakening the interconnectivity of the cementitious material<sup>36</sup>, which ultimately caused a decrease in mechanical strength.

As observed in Fig. 9c, with the increase of quicklime, the 7 d flexural strength initially increased and then decreased, while the 28 d flexural strength first decreased and then increased. When the quicklime dosage was 12%, the 7 d flexural strength reached the maximum 1.18 MPa, and at 16% quicklime dosage, the 28 d flexural strength peaked at 4.10 MPa. The main reason for the improvement of later flexural strength was the activation of the cementitious components by quicklime, which led to the formation of C-S-H and C-A-H, thereby enhancing the compactness of the cementitious material structure. After calcining at 105 °C, the cementitious activity of RM was enhanced. Under the effect of  $\text{OH}^-$  provided by quicklime hydrolysis, the Si-O and Al-O bonding on the surface of RM particles were broken (Fig. 10). The polymeric structures in RM, which were originally formed by  $[\text{SiO}_4]$  and  $[\text{AlO}_4]$  tetrahedra, split into monomers or dimers. These active units then underwent a series of depolymerization-repolymerization-condensation reactions in the presence of  $\text{Ca}(\text{OH})_2$ , forming zeolite-like structures<sup>37</sup>. The microstructural cementitious material condensed and hardened, and through the bonding effects of C-S-H, the mechanical properties were improved. Meanwhile, quicklime exhibited good water retention properties<sup>14</sup>, leading to the formation of a water film on its surface, which facilitated more complete reactions between the particles. Furthermore, the heat released by quicklime when it interacted with water further accelerated the hydration process. As a result, increasing the quicklime was beneficial for enhancing the flexural strength at later stages.

### Effect of cementitious components on the compressive strength

The effects of various cementitious components on the compressive strength of MS-RMCM are shown in Fig. 11. It can be seen that the effects of these components on the compressive strength at both early and later stages are similar.

From Fig. 11a, it can be seen that when the fly ash dosage was 15%, the compressive strength of the samples at both 7 d and 28 d reached their maximum, 15.53 MPa and 19.87 MPa, respectively. However, as the fly ash dosage continued to increase, the compressive strength at all ages gradually decreased. Figure 12 shows the

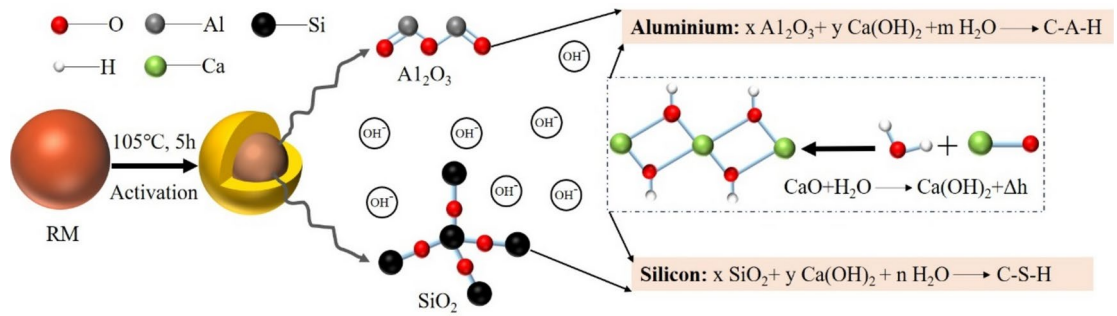


Fig. 10. Activation of RM.

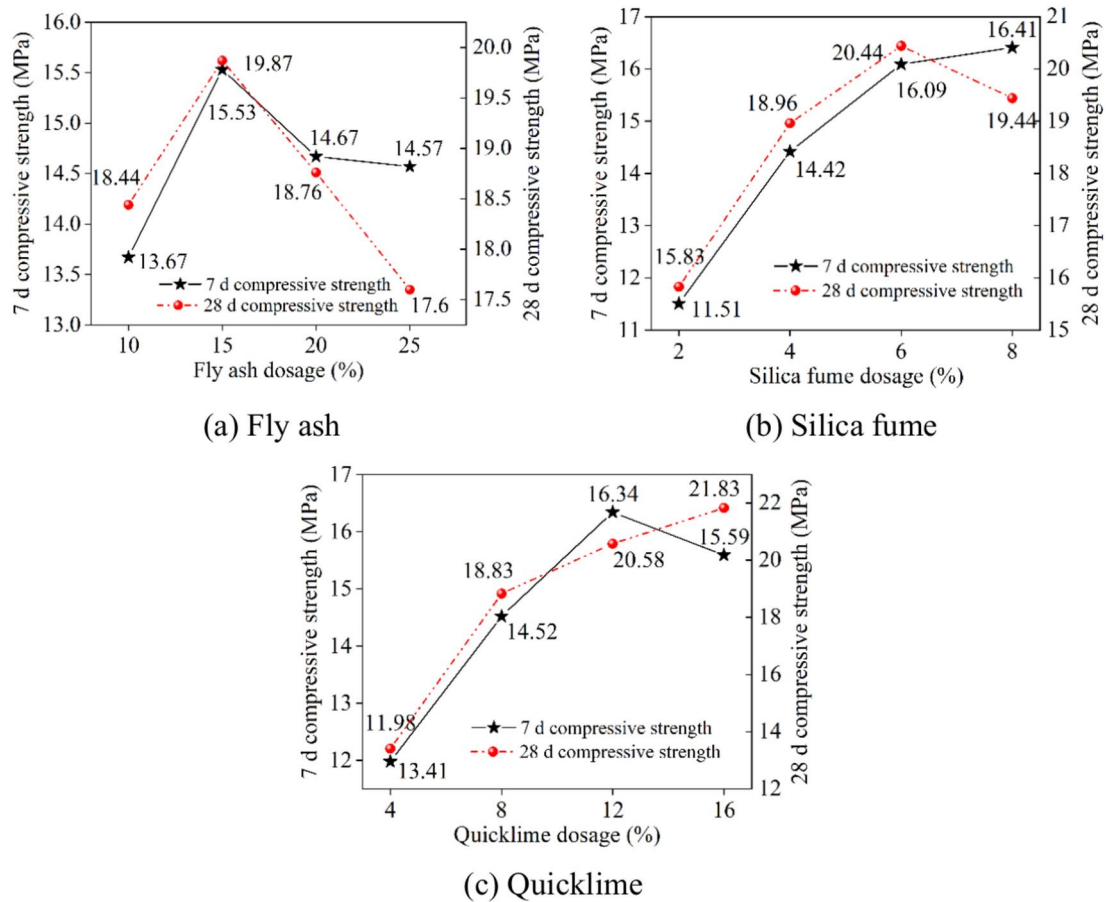
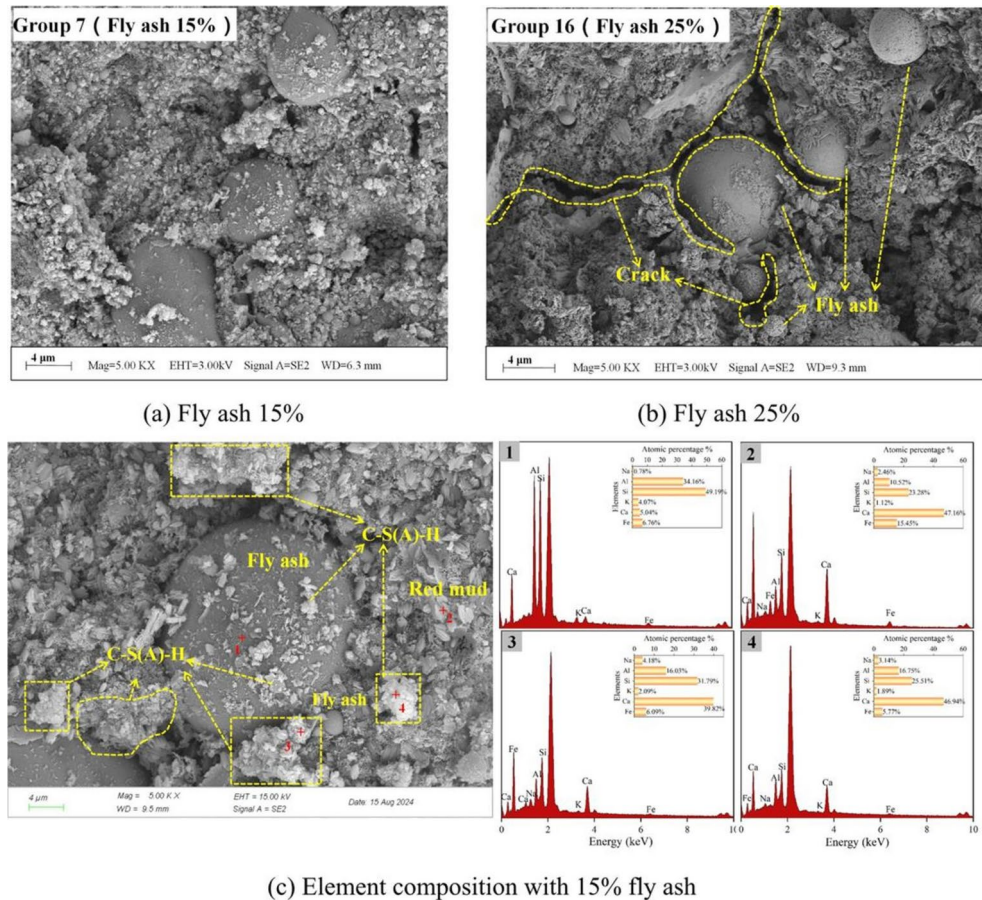


Fig. 11. Mean effect plots of 7 d and 28 d compressive strengths.

microstructure of the samples with 15% and 25% fly ash, as well as the element composition of the sample with 15% fly ash. When the fly ash dosage was 15%, the internal structure of the sample was compact, and a large number of spherical particles, block-shaped particles, and aggregates of gels and crystals presented within the cementitious material. Among these, the spherical and block-shaped particles formed the structural framework through the filling of hydration crystals. According to the EDS elemental analysis shown in Fig. 12c, the spherical particles were identified as unreacted fly ash. The block-shaped materials, containing more than 15% Fe, were determined to be RM. The aggregates of gels and crystals, which contained significant amounts of Ca, Al, and Si, as well as some Fe, were hypothesized to be a mixture of C-S-H, C-A-H, and C-A-F-H. This indicated that under the alkaline activation of quicklime, fly ash and other cementitious components generated a large amount of hydration gels and crystals, which enhanced the strength of the cementitious material. However, as the fly ash dosage increased, the quantity of unreacted fly ash particles gradually increased, while the hydration products were insufficient to fully fill the pores between the particles and the cementitious material. Furthermore, due to the lubricating properties of fly ash particles<sup>24</sup>, the bond strength between the unreacted particles and the



**Fig. 12.** SEM images and element composition of samples with various fly ash (Note: The unmarked peaks in the EDS represented Au element, which was the residual from the gold sputtering process used for testing. This applied to all similar instances).

cementitious material was insufficient. The large number of pores between the particles and the cementitious material developed into internal defects (as shown in Fig. 12b), which led to a macroscopic reduction in strength. It can thus be concluded that excessive fly ash reduced the bond strength and compactness of the cementitious material. Based on the above analysis, the optimal fly ash dosage was determined to be 15%.

As shown in Fig. 11b, with the increase of silica fume, the 7 d compressive strength gradually increased, while the 28 d compressive strength first increased and then decreased. When the silica fume dosage was 6%, the 28 d compressive strength reached its optimum 20.44 MPa, with an increase of 4.61 MPa. When the silica fume dosage was 8%, the 7 d compressive strength peaked at 16.09 MPa, with an increase of 4.90 MPa. This was attributed to the good latent pozzolanic activity and micro-aggregate filling effect of silica fume<sup>36</sup>, which effectively enhanced the compactness of the hardened material. Figure 13 shows the microstructure of specimens with different silica fume dosage and the element composition of the specimen with 6% silica fume. It can be observed that when the silica fume dosage was 2%, the internal structure of the cementitious material was loose. As the silica fume dosage increased to 6%, a large amount of C-S-H, C-A-H, and C-A-F-H mixtures formed within the material, tightly surrounding the unreacted silica fume particles and providing a bonding effect. Some of the C-A-H transformed into hydrogarnet ( $C_3AH_6$ ), and the unreacted silica fume particles filled the pores, enhancing the compactness of the cementitious material, thereby contributing to the improvement of compressive strength. After the silica fume dosage increased to 8% (Fig. 13c), the unreacted silica fume particles agglomerated, created isolation zones with either no or weak hydration bonding, which reduced the integrity of the cementitious material. As a result, the 28 d compressive strength decreased. This suggested that excessive silica fume was unfavorable for enhancing the later-stage strength. Based on this analysis, the optimal silica fume dosage was determined to be 6%.

Figure 11c shows the effect of quicklime on compressive strength. With the increase in quicklime dosage, the 7 d compressive strength initially increased and then decreased, while the 28 d compressive strength gradually increased. Compared with silica fume, quicklime had a more significant effect on improving compressive strength. At a quicklime dosage of 12%, the 7 d compressive strength peaked at 16.34 MPa, a 21.85% increase. At 16% quicklime dosage, the 28 d compressive strength reached its highest value of 21.83 MPa, an increase of 82.22%. In terms of early strength, excessive quicklime led to a reduction in the compressive strength. This was primarily due to the tendency of  $Ca(OH)_2$ , C-S-H, and RM particles to agglomerate during the early hydration

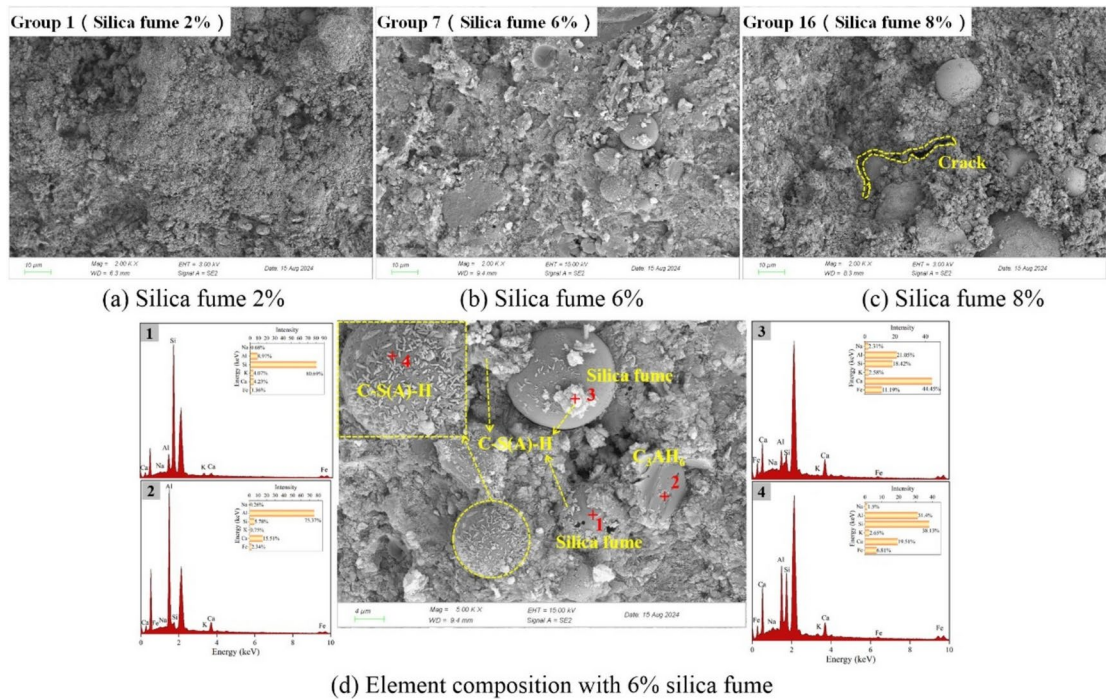


**Fig. 13.** SEM images and element composition of samples with various silica fume.

stage. The excessive  $\text{Ca}(\text{OH})_2$  weakened the strength of the cementitious material, making it less capable of resisting the external forces<sup>38</sup>. Moreover, the hydration of quicklime generated significant heat, creating thermal stress. This stress was unevenly distributed due to the effect of the pore structure<sup>39</sup>. When the thermal stress exceeded the internal bond strength, local defects developed within the cementitious material, leading to a decrease in strength. Figure 14 shows the microstructure and element composition of MS-RMCM specimens at different quicklime dosage. As seen in Fig. 14a,b, with increasing quicklime dosage, the cementitious material gradually became denser. When the quicklime dosage was 4%, the cementitious material contained numerous cracks and a limited amount of C-S-H. Due to the low quicklime dosage, the alkaline activation effect on silica fume, fly ash, and RM was poor, leading to the presence of a large number of unreacted particles within the cementitious material. When the quicklime dosage was 16%, the hydration products of silicoaluminate went through the depolymerization and re-polymerization under the effect of  $\text{OH}^-$ <sup>18</sup>. A three-dimensional network structure was formed, which continuously bonded and condensed, thereby enhancing the strength. At this point, the proportion of unreacted particles decreased, and some residual particles were tightly enveloped by the hydration products, contributing to the fine aggregate filling effect. This caused the internal structure to be more orderly and densely packed. Nevertheless, the formation of hydration products limited the reaction between  $\text{OH}^-$  and  $\text{SiO}_2$ ,  $\text{Al}_2\text{O}_3$ , resulting in excessive quicklime having a limited effect on improving the strength at later stages<sup>40</sup>. At the same time, the excessive quicklime generated a large amount of heat during hydration, which could lead to internal expansion and cracking. Based on the above analysis, the optimal quicklime dosage was identified as 16%.

### Carbon emissions analysis

The excessive emission of greenhouse gas makes the global climate problem increasingly serious. Carbon emissions reduction has become the urgent task to alleviate the current climate problems. In the context of low-carbon transformation of cement industry, developing low-carbon cementitious materials, especially the solid waste, has been the effective measure to reduce carbon emissions.

Based on the results of orthogonal tests, this paper selected the optimal mix ratio of 53% RM, 15% fly ash, 6% silica fume, and 16% quicklime as a case to calculate the  $\text{CO}_2$  emissions through the life cycle assessment method<sup>41</sup>. The study only considered carbon emissions during the preparation process of MS-RMCM, excluding the emissions related to its subsequent utilization and waste disposal processes. The total carbon emissions ( $S_{\text{CO}_2}$ ) from the preparation process primarily included emissions from raw material acquisition ( $A_{\text{CO}_2}$ ), emissions from raw material transportation ( $T_{\text{CO}_2}$ ), and emissions during preparation ( $P_{\text{CO}_2}$ ). The carbon emissions are calculated by the below Eqs. <sup>42</sup>.

$$S_{\text{CO}_2} = A_{\text{CO}_2} + T_{\text{CO}_2} + P_{\text{CO}_2} \tag{3}$$

$$A_{\text{CO}_2} = \sum M_i \times E_i \tag{4}$$

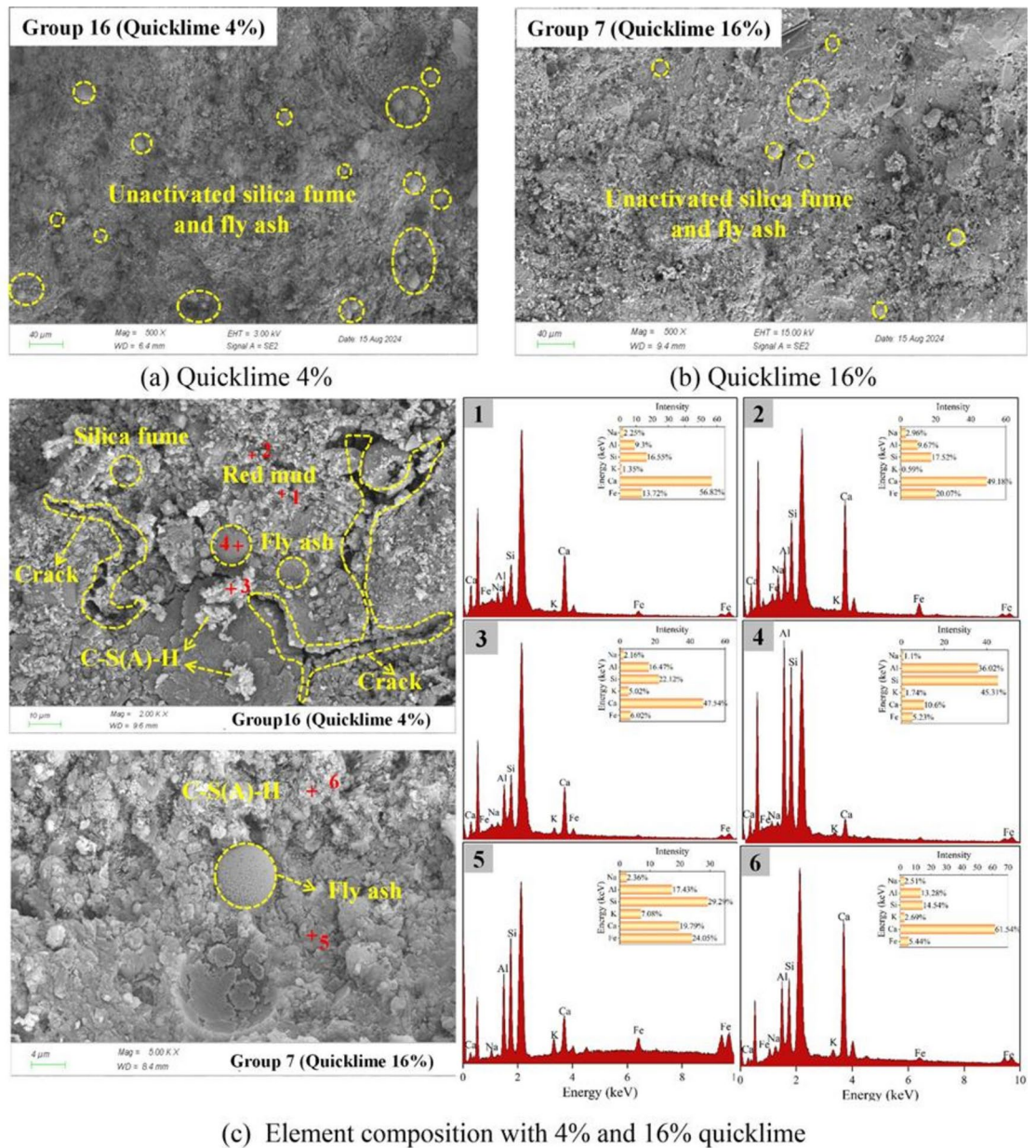


**Fig. 14.** SEM images and element composition of samples with various quicklime.

$$T_{CO_2} = \sum M_i \times D_i \times TE_i \tag{5}$$

$$P_{CO_2} = \sum M_i \times El_i \times EE_i \tag{6}$$

In the above equations,  $M_i$  represents the mass of  $i$  raw material in 1 ton of MS-RMCM,  $t$ ;  $E_i$  denotes the carbon emission factor of the  $i$  raw material,  $kg/t$ ;  $D_i$  is the transport distance,  $km$ ;  $TE_i$  indicates the carbon emission coefficient during transportation,  $kg/(t \cdot km)$ ;  $El_i$  represents the electricity consumption in processing 1 ton of  $i$  raw material,  $kWh/t$ ;  $EE_i$  refers to the carbon emission factor for electricity consumption,  $kg/kWh$ .

Since RM was an industrial solid waste, the raw material acquisition process was assumed to have no carbon emissions<sup>12</sup>. According to Eq. (4), the total carbon emissions in acquisition 1 ton of raw materials for MS-RMCM amounted to 266.29 kg, as shown in Table 7.

The transportations of RM, fly ash, and other cementitious components, as well as additives, were primarily carried out by 30-ton heavy-duty diesel trucks. Referring to Chinese standard GB/T 51,366–2019 "Calculation Standards of Building Carbon Emissions", the carbon emission factor was determined to be 0.078  $kg/(t \cdot km)$ . Based on Eq. (5), the total carbon emissions generated during the raw material transportation stage were 4.79 kg, with the calculation results presented in Table 8.

Raw materials	RM	Fly ash	Silica fume	Quicklime	Cement	Water reducer	Water
Mix ratio/%	53	15	6	16	10	1	40
Mass $M_i$ /t	0.53	0.15	0.06	0.16	0.1	0.01	0.4
Carbon emission factors $E_i$ kg/t	0 <sup>12</sup>	8 <sup>44</sup>	14 <sup>45</sup>	1190 <sup>43</sup>	735 <sup>43</sup>	28.50 <sup>44</sup>	0.17 <sup>43</sup>
$A_{CO_2}$ /kg	0	1.20	0.84	190.40	73.50	0.29	0.07

**Table 7.** CO<sub>2</sub> emissions in acquisition 1 ton of raw materials for MS-RMCM (kg).

Raw materials	RM	Fly ash	Silica fume	Quicklime	Cement	Water reducer	Water
Mass $M_i$ /t	0.53	0.15	0.06	0.16	0.1	0.01	0.4
Distance $D_i$ /km	55	170	15	10	40	20	0
Carbon emission factor $TE_i$ kg/(t·km)	0.078 <sup>43</sup>						
$T_{CO_2}$ /kg	2.274	1.989	0.070	0.125	0.312	0.016	0

**Table 8.** CO<sub>2</sub> emissions in transportation 1 ton of raw materials for MS-RMCM (kg).

Raw materials	Mix ratio/%	Mass $M_i$ /t	Process	Electricity consumption $E_i$ kWh/t	Carbon emission factor $EE_i$ kg/kWh	$P_{CO_2}$ /kg
RM	53	0.53	Crushing	3.33	0.942 <sup>12</sup>	1.663
			Sieving	0.53		0.265

**Table 9.** CO<sub>2</sub> emissions in preparation 1 ton of raw materials for MS-RMCM (kg).

The carbon emissions during the preparation stage primarily resulted from the activation treatment of RM which included crushing and screening processes. Other materials were finished products and could be directly used for production. According to the official website of the Ministry of Ecology and Environment of the People's Republic of China, the carbon emission factor for electricity consumption was found to be 0.942 kg/kWh. Based on Eq. (6), the total carbon emissions during the raw materials preparation stage were 1.93 kg, as shown in Table 9.

According to Eq. (3), the total carbon emissions from producing 1 ton of MS-RMCM amounted to 273.01 kg, with a carbon emission factor of 0.273 kg/kg. The carbon emissions of high-dosage RM-based cementitious materials primarily originated from the raw material acquisition stage, contributing 266.29 kg CO<sub>2</sub>, which accounted for approximately 97.54% of the total emissions. Among these, quicklime accounted for 71.50% of the raw material carbon emissions, while cement contributed 27.60%. When the RM was entirely replaced with cement, the total carbon emissions increased to 660.01 kg, indicating that replacing cement with RM reduced CO<sub>2</sub> emissions by 58.64%.

To further analyze the CO<sub>2</sub> reduction effect of the MS-RMCM, the carbon emissions per compressive strength were used as an indicator to compare the emissions data of red mud-based cementitious materials. As shown in Fig. 15, based on the Chinese standard GB/T 51,366–2019 "Calculation Standards of Building Carbon Emissions", the carbon emissions of cement were 735 kg/t. Compared with cementitious materials RM-WGS made from RM and waste glass sludge<sup>46</sup>, the MS-RMCM in this study reduced CO<sub>2</sub> emissions per compressive strength by 49.30%. Shi et al.<sup>47</sup> reported that the carbon emissions of RM-GGBS cementitious materials prepared with RM and ground granulated blast-furnace slag reached 599.40 kg/t, primarily due to the use of sodium silicate as an activator during preparation, which significantly increased CO<sub>2</sub> emissions. Additionally, while Zhang<sup>48</sup> reported that RM-based sulphoaluminate cementitious materials (RS) exhibited lower carbon emissions per compressive strength than those in this study, the preparation process involved high-temperature calcination, leading to complex procedures and higher initial equipment investment. Therefore, the MS-RMCM in this study not only achieved large-scale consumption of RM but also demonstrated significant advantages in CO<sub>2</sub> reduction.

## Conclusions

In this study, fly ash, silica fume, quicklime, and cement were added to RM to prepare multi-solid-waste synergistic red mud-based composite cementitious materials (MS-RMCM). Orthogonal tests were conducted to investigate the effects of various cementitious components on the flexural and compressive strengths. The mean effect plots were utilized to identify the effect trends and appropriate values of each component, providing a basis for selecting admixtures in the research of RM-based cementitious materials. Additionally, microscopic analysis was employed to reveal the mechanism of each cementitious component. On the basis of optimal mix ratio, the CO<sub>2</sub> emissions analyses were carried out. The RM utilization rate in the cementitious material reached 45%–75%, achieving large-scale and resource-efficient utilization of RM in the construction industry. The main conclusions are summarized as follows:

- (1) The effects of fly ash, silica fume, and quicklime on the flexural and compressive strengths of MS-RMCM vary with curing age. For the 28 d compressive strength, the degree of effect of each factor is ranked as

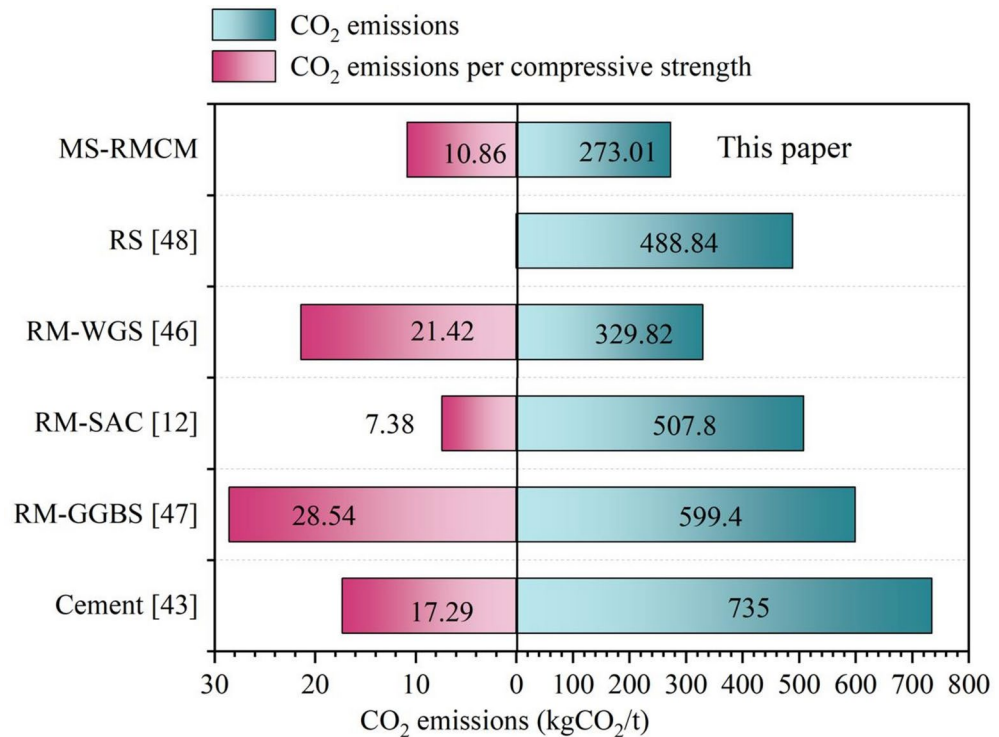


**Fig. 15.** Carbon emissions comparison.

follows: quicklime (C) > silica fume (B) > fly ash (A). The optimal combination is determined to be  $A_2B_3C_4$ , achieving a maximum compressive strength of 25.13 MPa with 53% RM. For the 28 d flexural strength, the ranking is: fly ash (A) > quicklime (C) > silica fume (B), with the optimal combination identified as  $A_4B_1C_4$ . Variance analysis reveals that the effects of fly ash on both compressive and flexural strengths are not significant, while the effect of silica fume on compressive strength is highly significant. The effect of quicklime on the 28 d compressive strength is more significant than the effect at 7 d.

- (2) The compressive strength and early flexural strength exhibit a trend of first increasing and then decreasing with the increase of fly ash. When the fly ash dosage is 15%, the compressive strength at 7 d and 28 d, as well as the 7 d flexural strength, reaches their maximum of 15.53 MPa, 19.87 MPa, and 1.10 MPa, respectively. Based on a comprehensive evaluation of the compressive and flexural performances, the optimal dosage of fly ash is identified as 15%.
- (3) The addition of silica fume enhances the 7 d compressive and flexural strengths. However, the 28 d compressive strength shows an initial increase followed by a decrease as the silica fume increases. At a silica fume dosage of 6%, the 28 d compressive strength reaches the maximum (20.44 MPa), which is attributed to the high potential pozzolanic activity and micro-filler effect of silica fume. Conversely, excessive silica fume causes the unreacted particles to aggregate, forming weakly hydrated zones that reduce the compactness of the cementitious material. Therefore, the optimal silica fume dosage is determined to be 6%.
- (4) Quicklime positively contributes to the development of both flexural and compressive strengths, with greater increase in later strength observed as the quicklime dosage increases. When the quicklime dosage reaches at 16%, the 28 d flexural and compressive strengths reach their maximums of 4.10 MPa and 21.83 MPa, respectively. The strength improvements are primarily attributed to the activation of the cementitious components by quicklime, which facilitates the formation of C-S-H that filled the original pores, thereby increasing the compactness. Considering the expansion and cracking caused by excessive hydration heat, the optimal quicklime dosage is determined to be 16%.
- (5) Using the optimal combination from the orthogonal tests as a case, the total life-cycle CO<sub>2</sub> emissions of MS-RMCM are calculated, and the CO<sub>2</sub> reduction effect of the material is assessed based on the carbon emissions per compressive strength. The carbon emissions from producing 1 ton of MS-RMCM are 273.01 kg, with a carbon emission coefficient of 10.86 kg/MPa. By substituting RM for cement, the CO<sub>2</sub> emissions are reduced by 58.64%, highlighting the significant CO<sub>2</sub> reduction advantages of MS-RMCM in the construction industry.

### Data availability

All data generated or analyzed during this study are included in this article, the data used in this paper are original data. And the datasets used and/or analyzed during the current study available from the corresponding author on reasonable request.

Received: 29 November 2024; Accepted: 21 January 2025

Published online: 24 January 2025

## References

- Ren, C. D. et al. Performance study and effect mechanism of red mud manufactured sand foam concrete using a single-factor experiment. *Constr. Build. Mater.* **458**, 139629 (2024).
- Arroyo, F., Luna-Galiano, Y., Leiva, C., Vilches, L. F. & Fernández-Pereira, C. Environmental risks and mechanical evaluation of recycling red mud in bricks. *Environ. Res.* **186**, 109537 (2020).
- Karimipour, A., Jahangir, H. & Eidgahee, D. R. A thorough study on the effect of red mud, granite, limestone and marble slurry powder on the strengths of steel fibres-reinforced self-consolidation concrete: Experimental and numerical prediction. *J. Build. Eng.* **44**, 103398 (2021).
- Song, Y. F. et al. Effects of red mud on workability and mechanical properties of autoclaved aerated concrete (AAC). *J. Build. Eng.* <https://doi.org/10.1016/j.job.2022.105238> (2022).
- Shu, J. et al. Performance and microstructure of red-mud-blended concrete under different aqueous environments. *Constr. Build. Mater.* **447**, 137988 (2024).
- Hao, X. S. et al. In-depth insight into the cementitious synergistic effect of steel slag and red mud on the properties of composite cementitious materials. *J. Build. Eng.* **52**, 104449 (2022).
- Pan, Z. H., Cheng, L., Lu, Y. N. & Yang, N. R. Hydration products of alkali-activated slag–red mud cementitious material. *Cem. Concr. Res.* **32**, 357–362 (2002).
- An, Y. X. et al. An efficient and clean utilization technique for red mud based on fluidized bed carbon monoxide reduction. *Adv. Powder Technol.* **33**, 103828 (2022).
- Zhang, N. et al. Effects of low- and high-calcium fly ash on the water resistance of magnesium oxysulfate cement. *Constr. Build. Mater.* **230**, 116951 (2020).
- Li, B. et al. Simultaneous removal of SO<sub>2</sub> and NO using a novel method with red mud as absorbent combined with O<sub>3</sub> oxidation. *J. Hazard. Mater.* **392**, 122270 (2020).
- Gonçalves, N. P. F., Olhero, S. M., Labrincha, J. A. & Novais, R. M. 3D-printed red mud/metakaolin-based geopolymers as water pollutant sorbents of methylene blue. *J. Clean. Prod.* **383**, 135315 (2023).
- Zhang, C. Experimental study on preparation and application of high strength cold bonded lightweight aggregates based on two-step transition utilization of red mud together with multi-source solid wastes. <https://doi.org/10.27272/d.cnki.gshdu.2023.007120> (In Chinese) (2023).
- Wei, B., Zhang, Y. M. & Bao, S. X. Mechanical activation to improve activity of vanadium tailing from stone coal. *Metal Mine.* **2**, 188–192 (2017) ((In Chinese)).
- Jiang, C. C. & Li, G. Z. Study on light porous unsintered building material. *Adv. Mater. Res.* **549**, 144–148. <https://doi.org/10.4028/www.scientific.net/AMR.532-533.144> (2012).
- Kanagaraj, B., Anand, N., Samuvel Raj, R. & Lubloy, E. Performance evaluation on engineering properties of sodium silicate binder as a precursor material for the development of cement-free concrete. *Dev. Built Env.* **12**, 100092 (2022).
- Kanagaraj, B., Anand, N., Samuvel Raj, R. & Lubloy, E. Performance evaluation of sodium silicate waste as a replacement for conventional sand in geopolymer concrete. *J. Clean. Product.* **375**, 134172 (2022).
- Li, S. C., Zhang, G. L., Zhao, T. J., Wang, H. T. & Jin, Z. Q. Effect of activation mode of Bayer red mud on properties of cement-based materials. *Concrete* **6**, 29–32 (2013) ((In Chinese)).
- Xue, S. G. et al. Research progress of red mud in gelling materials and road applications. *Chin. J. Nonferrous Metals.* **33**, 3421–3439 (2023) ((In Chinese)).
- Kanagaraj, B. et al. Investigation of physical, chemical, mechanical, and microstructural properties of cement-less concrete—state-of-the-art review. *Constr. Build. Mater.* **365**, 130020 (2022).
- Liu, J. X., Li, Z. Y., Zhang, M. L., Wang, S. Q. & Hai, R. Mechanical properties and polymerization mechanism of red mud polymer cement. *J. Build. Mater.* **25**, 178–183 (2022) ((In Chinese)).
- Geng, J. J. et al. Comparison of red mud and coal gangue blended geopolymers synthesized through thermal activation and mechanical grinding preactivation. *Constr. Build. Mater.* **153**, 185–192 (2017).
- Bao, S. X., Qin, L., Zhang, Y. M., Luo, Y. P. & Huang, X. L. A combined calcination method for activating mixed shale residue and red mud for preparation of geopolymer. *Constr. Build. Mater.* **297**, 123789 (2021).
- Deng, Y. Y., Wang, X. C., Zhou, B., Xu, X. J. & Chen, L. Systematic assessment of a multi-solid waste cementitious material: Feasibility and environmental impact. *Constr. Build. Mater.* **428**, 136323 (2024).
- Li, Y. et al. Preparation, characterization and application of red mud, fly ash and desulfurized gypsum based eco-friendly road base materials. *J. Clean. Product.* **284**, 124777 (2021).
- Luo, Z. T. et al. Solidification/stabilization of chromium slag in red mud-based geopolymer. *Constr. Build. Mater.* **316**, 125813 (2022).
- Wang, R. Q. et al. Study on the design method of multi-component industrial solid waste low carbon cementitious material with cement as the activator. *Case Stud. Constr. Mater.* **21**, e03478 (2024).
- Kirthiga, R. & Elavenil, S. Potential utilization of sugarcane bagasse ash in cementitious composites for developing inorganic binder. *Ain Shams Eng. J.* **14**, 102560 (2023).
- Ding, Z. Y., Cheng, Y., Jin, L., Wang, W. T. & Yan, S. Y. Study on the strength characteristics and micro-mechanism of modified solidified red mud. *J. Front. Mater.* **11**, 1461198 (2024).
- He, G. L., Cui, W. W., Yang, Z., Zhao, R. Y., Dong, X. Q. Research on basic engineering properties of alkali-activated red mud solidified by slag and silica fume. *J. Taiyuan Univ. Technol.* 1–11; <http://kns.cnki.net/kcms/detail/14.1220.N.20231221.1114.002.html>. (In Chinese) (2024).
- Liu, C. H., Yue, X. T., Jiao, C. B., Zhao, Y. L. & Zhang, X. B. Preparation and properties of red mud based cementitious materials. *Bull. Chin. Silic. Soc.* **39**, 3574–3581 (2020) ((In Chinese)).
- Dong, M. H. et al. Size distribution of pores and their geometric analysis in red mud-based autoclaved aerated concrete (AAC) using regression neural network and elastic mechanics. *Constr. Build. Mater.* **359**, 129420 (2022).
- Ministry of machinery industry of the people's republic of China. JB-T7510-1994 "Process parameter optimization method orthogonal test method" (Chinese standard) (1994).
- Xu, C. W. et al. Hydration mechanism and orthogonal optimisation of mix proportion for steel slag-slag-based clinker-free prefabricated concrete. *Constr. Build. Mater.* **228**, 117036 (2019).
- Que, L. L., Zhu, J. L., Wang, F. & Li, Z. R. Mechanical properties of polyethylene fiber reinforced red mud-alkali slag composite materials. *J. Compos. Mater.* **39**, 5367–5374 (2022) ((In Chinese)).
- Liu, A. et al. Mechanical properties and microscopic mechanism of basalt fiber-reinforced red mud concrete. *Constr. Build. Mater.* **416**, 135155 (2024).
- Wang, S. N. et al. Strength performance and enhancement mechanism of silty sands stabilized with cement, red mud, and phosphogypsum. *J. Build. Eng.* **73**, 106762 (2023).
- Duxson, P. et al. Geopolymer technology: the current state of the art. *J. Mater. Sci.* **42**, 2917–2933. <https://doi.org/10.1007/s10853-006-0637-z> (2007).

38. Yang, Z. Q. & Guo, J. Y. Study on mechanical properties and microscopic mechanism of lime treated soil. *Rock Soil Mech.* **3**, 11–23 (1991) **(In Chinese)**.
39. Qu, X. L. et al. Heat release characteristics of lime and time-dependent rheological behaviors of lime-activated fly ash pastes. *Case Stud. Constr. Mater.* **16**, e01043 (2022).
40. Xu, X., Fan, X. L. & Yang, C. L. Investigation on physical properties, strength and phase evolution of binary cementitious materials made of CFBC ash and lime. *Constr. Build. Mater.* **265**, 120302 (2020).
41. Kanagaraj, B., Anand, N., Samuvel Raj, R. & Lubloy, E. Techno-socio-economic aspects of portland cement, geopolymers, and limestone calcined clay cement (LC3) composite systems: A-State-of-Art-Review. *Constr. Build. Mater.* **398**, 132484 (2023).
42. Wang, X. J. et al. Quantification of CO<sub>2</sub> emission from the preparation and utilization of solid waste-based sulphoaluminate cementitious materials. *J. Clean. Product.* **376**, 134054 (2022).
43. Xu, W. et al. GB/T 51366–2019 “Calculation Standards of Building Carbon Emissions” (Chinese standard) (2019).
44. Jin, B. Research on low carbon concrete ratio based on low cement dosage. <https://doi.org/10.27398/d.cnki.gxalu.2024.000280>. (In Chinese) (2024).
45. Jia, C.X. Quantitative analysis of carbon emission of 3D printing building structure based on life cycle assessment. <https://doi.org/10.27461/d.cnki.gzjdx.2021.002813>. (In Chinese) (2021).
46. Li, Y. X. et al. Preparation of environmental-friendly cementitious material from red mud and waste glass sludge by mechanical activation. *Constr. Build. Mater.* **423**, 135861 (2024).
47. Shi, J. M. et al. Upcycling use of red mud-based solid waste in engineered cementitious composites: Properties, activation mechanism, and life-cycle assessment. *J. Clean. Product.* **447**, 141504 (2024).
48. Zhang, C. et al. Collaborative recycling of red mud and FGD-gypsum into multi-shell cold bonded lightweight aggregates: Synergistic effect, structure design and application in sustainable concrete. *Constr. Build. Mater.* **379**, 131134 (2023).

## Acknowledgements

The authors gratefully acknowledge the support provided by the National Natural Science Foundation of China (No. 12362011) and Natural Science Research Program of Guizhou Education Department (No. [2024]276).

## Author contributions

Lili Cheng: Conceptualization, Methodology, Investigation, Funding acquisition, Writing original draft. Daiyu Zhou: Methodology and Validation. Qiwan Zhang: Experimental test, Investigation. Lingling Wang: Funding acquisition, Resources, Reviewing and Editing. Ninggui Hu and Zeyuan Wang: Experimental assistance.

## Declarations

### Competing interests

The authors declare no competing interests.

### Additional information

**Correspondence** and requests for materials should be addressed to L.C.

**Reprints and permissions information** is available at [www.nature.com/reprints](http://www.nature.com/reprints).

**Publisher’s note** Springer Nature remains neutral with regard to jurisdictional claims in published maps and institutional affiliations.

**Open Access** This article is licensed under a Creative Commons Attribution-NonCommercial-NoDerivatives 4.0 International License, which permits any non-commercial use, sharing, distribution and reproduction in any medium or format, as long as you give appropriate credit to the original author(s) and the source, provide a link to the Creative Commons licence, and indicate if you modified the licensed material. You do not have permission under this licence to share adapted material derived from this article or parts of it. The images or other third party material in this article are included in the article’s Creative Commons licence, unless indicated otherwise in a credit line to the material. If material is not included in the article’s Creative Commons licence and your intended use is not permitted by statutory regulation or exceeds the permitted use, you will need to obtain permission directly from the copyright holder. To view a copy of this licence, visit <http://creativecommons.org/licenses/by-nc-nd/4.0/>.

© The Author(s) 2025